A Simple Numerical Model to Estimate the Temperature Distributions Over Photodetectors in Steady-State

Ergun Simsek, *Senior Member, IEEE,* Alexander S. Hastings, David A. Tulchinsky, *Member, IEEE,*, Keith J. Williams, and Curtis R. Menyuk, *Life Fellow, IEEE,*

***Abstract*—This research introduces an approximation method for computing the temperature distribution in photodetectors operating in a steady state under optical excitation. The derived temperature profile is utilized to assess the impact of temperature variations on crucial performance metrics of photodetectors, encompassing quantum efficiency, bandwidth, and phase noise. Our methodology, grounded in simplified heat transport equations, yields significant insights into the intricate relationship between temperature and photodetector performance. Our findings reveal that assuming constant room temperature operation leads to an overestimate of the output current and quantum efficiency and an underestimate of bandwidth, by contrast, a model in which the temperature varies produces estimates that closely align with experimentally-measured values for quantum efficiency and bandwidth. The low thermal conductivity of InGaAs hampers heat dissipation, resulting in temperature accumulation. Varying the reverse bias voltage while keeping the output current constant by changing the input optical power leads to nonlinear variations in the bandwidth, phase noise, and quantum efficiency. These insights contribute to the understanding and optimization of thermal management in photodetectors under strong optical excitations.**

***Index Terms*—photodetectors, photodiodes, thermal modeling.**

I. Introduction

Photodetectors (also known as photodiodes and abbreviated as PDs in the rest of the document) are critical components in microwave photonics [1]–[11]. These devices have led to substantial improvements in key performance parameters such as link gain, noise figure, and spurious free dynamic range. However, the realization of elevated radio frequency (RF) output power encounters challenges primarily stemming from saturation effects induced by the space-charge effect [1], [6] and the risk of heat-induced catastrophic failure [10], [11].

Uni-traveling carrier (UTC) PDs have successfully addressed the space-charge effect, demonstrating enhanced high-power performance in comparison to traditional p-i-n PDs, while maintaining high speed and linearity [2]. The introduction of modified uni-traveling carrier (MUTC) PDs, featuring a distinctive cliff layer controlling the electric field strength in absorber and collector regions, has further improved space-charge tolerance [3]–[5]. In [3], the researchers found out that the responsivity of both UTC and MUTC PDs increased as a result of the increased photoabsorption coefficient at elevated operating temperatures. However, the temperature-dependent bandwidths behaved differently depending on the thicknesses of the p and i layers due to competing effects such as reduced carrier saturation velocity in the undoped or lightly-doped photoabsorption layer and increased electron diffusion in the p-type layer at higher temperatures [3].

Despite these advances, the pursuit of higher RF output power has been hampered by thermal challenges. This paper explores the thermal characteristics of conventional backside-illuminated MUTC PDs, with a primary focus on the MUTC2 variant [5]. Notably, this PD has achieved remarkable results, including quantum efficiency of 0.55 and bandwidth of 24– GHz [5]. In another study [4], the researchers used a thermal-reflectance imaging system to characterize the surface temperature of the MUTC2. They also implemented a simulation model, using a commercially available finite element analysis tool and they obtained numerical results that are in good agreement with the measured results for the temperature distribution over the top surface of the PD. In another study, the researchers examined another variant of MUTC PD at three temperature regimes (300 K, 80 K, and 4 K) and multiple bias conditions [8]. They found out that both the responsivity and bandwidth decrease with decreasing temperature. There are also so many other publications presenting experimental [12]–[17] and/or numerical [18]–[21] results on the characterization of other types of PDs (such as $p-i-n$ and Avalanche PDs) as a function of temperature. When we examine the numerical models, we observe two distinct groups. In the first group of studies [19], [20], the temperature of the entire PD is set to a constant T value and the various number of calculations are carried out by assuming different T values. This approach might work well enough for simple PDs such as $p-i-n$ but definitely this is not a safe choice for PDs with many layers of semiconducting materials. In the second set of studies [12]–[14], [18], the temperature is included in the numerical model as one of the unknown parameters. The temperature that varies locally affects not only the material properties but also carrier concentrations, fields, and currents. Indeed, this is a thorough and reliable approach, however, in this work we are interested in a much more simplified approach to estimate the temperature distribution within the PDs with the hope of providing valuable insights into the temperature-dependent performance of PDs.

E. Simsek and C. R. Menyuk are with the Department of Computer Science and Electrical Engineering, University of Maryland Baltimore County, Baltimore, MD 21250, USA. A. S. Hastings, D. A. Tulchinsky, and K. J. Williams are with the U.S. Naval Research Laboratory, Washington, DC 20375 USA. Corresponding author's email: simsek@umbc.edu

Manuscript received February 22, 2024; revised ...

In the subsequent sections, we present our methodology, numerical results, and the implications of our findings for the further improvement of high-power PDs in future photonic microwave applications. Additionally, we delve into the temperature-dependent changes observed in quantum efficiency, RF output power, and bandwidth, as revealed by previous experimental studies. The implementation of a numerical model for temperature dependence allows us to explore the impact of temperature on the performance metrics of MUTC2 PD, paving the way for a comprehensive understanding of the thermal challenges associated with these advanced devices.

II. Numerical Model

We solve drift-diffusion equations to study PDs [22], [23], which start with the electron and hole continuity equations and the Poisson equation,

$$\frac{\partial(p - N_A^-)}{\partial t} = -\frac{1}{q}\nabla \cdot \mathbf{J}_p + G_{\text{ii}} + G_{\text{opt}} - R(n,p), \quad (1a)$$

$$\frac{\partial(n - N_D^+)}{\partial t} = +\frac{1}{q}\nabla \cdot \mathbf{J}_n + G_{\text{ii}} + G_{\text{opt}} - R(n,p), \quad (1b)$$

$$\nabla \cdot \mathbf{E} = \frac{q}{\epsilon}\left(n - p + N_A^- - N_D^+\right), \quad (1c)$$

where n is the electron density, p is the hole density, t is time, q is the unit of charge, $\mathbf{J}_n$ is the electron current density, $\mathbf{J}_p$ is the hole current density, R is the recombination rate, G_{ii} and G_{opt} are impact ionization and optical generation rates, $\mathbf{E}$ is the electric field at any point in the device, ϵ is the electrical permittivity, N_A^- is the ionized acceptor concentration, and N_D^+ is the ionized donor concentration. Further details of the formulation and broadband radio frequency (RF) output calculations in a single simulation can be found in [22] and [23], respectively. Here, we want to describe a simple addition to our drift-diffusion equations solver to estimate the temperature distribution over a photodetector. While the approach is validated for several PD types, we focus here on one particular design, referred to as MUTC2 in [4], [5]. The semiconductor material and dopant types, doping concentrations, and thickness of each layer are provided in Table I.

The heat transport equation, which describes the spatiotemporal dynamics of the temperature distribution in the photodetector, can be expressed as:

$$c_H \frac{\partial T}{\partial t} - \nabla \cdot \sigma_T \nabla T = H \quad (2)$$

where T is the temperature, c_H represents the volumetric heat capacity, σ_T denotes the thermal conductivity, and H signifies the heat generation rate. As listed in Table I, the photodetector comprises InP, InGaAs, and InGaAsP layers. The values of c_H and σ_T for these materials are provided in Table II.

We use a temperature-dependent thermal conductivity model for InGaAs given by the following equation

$$\sigma_T(T) = \sum_{i=1}^{3} a_i \exp\left(-\frac{(T - b_i)^2}{c_i^2}\right), \quad (3)$$

since the absorption occurs in the InGaAs layers, where the electric field is expected to be strong.

TABLE I
MUTC photodiode structure: semiconductor material type and thickness of each layer, their doping concentrations, and the type of dopants. This photodiode is referred as MUTC2 in [4], [5]. The diameter of the photodiode is 34 μm. The wavelength of the optical excitation is 1550 nm.

Material	Thickness (nm)	Doping Conc. (cm^{-3})	Dopant Type
InGaAs	50	2.0×10^{19}	Zn
InP	100	1.5×10^{18}	Zn
InGaAsP Q1.1	15	2.0×10^{18}	Zn
InGaAsP Q1.4	15	2.0×10^{18}	Zn
InGaAs	100	2.0×10^{18}	Zn
InGaAs	150	1.2×10^{18}	Zn
InGaAs	200	8.0×10^{17}	Zn
InGaAs	250	5.0×10^{17}	Zn
InGaAs	150	1.0×10^{16}	Si
InGaAsP Q1.4	15	1.0×10^{16}	Si
InGaAsP Q1.1	15	1.0×10^{16}	Si
InP	50	1.4×10^{17}	Si
InP	900	1.0×10^{16}	Si
InP	100	1.0×10^{18}	Si
InP	900	1.0×10^{19}	Si
InGaAs	20	1.0×10^{19}	Si
InP	200	1.0×10^{19}	Si

TABLE II
Heat capacitance and thermal conductivity of semiconducting materials that are used in the MUTC design detailed in Table I.

Material	c_H (J/gK)	σ_T (W/cmK)
InGaAs	0.3	See Eq. (3)
$\text{Ga}_{0.47}\text{In}_{0.53}\text{As}_y\text{P}_{1-y}$	$0.31 + 0.038y$ $-0.008y^2$	$0.68 - 1.77y$ $+1.25y^2$
InP	$0.28 + 10^{-4}T$	$0.68(300/T)^{1.4}$

The coefficients of this equation are extracted from the experimentally measured results provided in [24]. Figure 1 shows the good agreement between the measurement results and the ones obtained with Eq. (3). The bandgaps of the semiconductors [25], number of electrons and holes in the conduction and valence band [26], and low-field mobilities [27] and saturated velocities [28] of the holes and electrons are also calculated functions of temperature.

TABLE III
The coefficients used in Eq. (3) to calculate the thermal conductivity of InGaAs as a function temperature, T.

i	a_i	b_i	c_i
1	0.6204	194.1	86.21
2	1.159	197	180.9
3	4.959	-9.86	1044

Note that Eq. (2) requires the inclusion of boundary conditions. Moreover, for a time-dependent study, one must consider interfaces and numerous complex mechanisms. Nevertheless, if one aims to obtain an approximate temperature distribution for a photodetector in steady state, Eq. (2) can be simplified into the following expression, assuming that Joule heating is the primary heat source:

$$-\nabla \cdot \sigma_T \nabla T = \mathbf{J} \cdot \mathbf{E} \quad (4)$$

where $\mathbf{J}$ represents the local electric current. When utilizing many thin layers, each with a thickness of δz to describe a

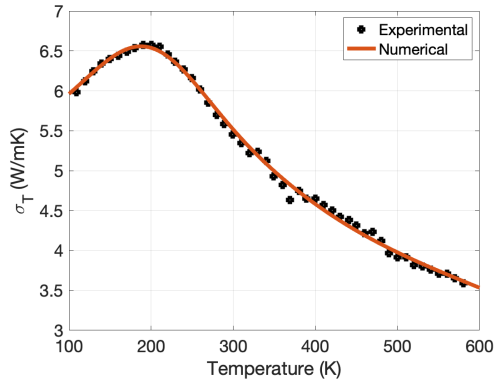

Fig. 1. Thermal conductivity of InGaAs as a function of temperature. The red curve is obtained with the Eq. (3) using the coefficients listed in Table III. The experimental results are taken from [24].

layer of a semiconductor device (where $\delta z \ll \lambda$), this simplified expression indicates that the local temperature change in the i^{th} thin layer can be approximated as:

$$\nabla T_i \approx -\frac{\delta z}{\sigma_T}(\mathbf{J} \cdot \mathbf{E}) \tag{5}$$

By assuming a constant temperature such as room temperature at the p-contact (because the photodetector is illuminated from the n-side), we effectively impose a Dirichlet boundary condition at $z = 0$. Furthermore, employing Eq. (5), wherein we approximate the derivative of temperature with a simple term, imposes a Neumann boundary condition at each interface of the 1D-mesh.

It should also be noted that in our iterative approach, as explained below, we use Eq. (5) for each layer of our 1D mesh and update the local temperature in each iteration. The material properties, such as thermal conductivity, heat capacity, electron and hole diffusion coefficients, mobilities, velocities, band gap, and electrical permittivity, are recalculated using the updated local temperature for each layer. The complete set of formulas used for temperature-dependent material modeling can be found in [22], [23], [27], [28].

III. Numerical Results

For all the numerical results presented here, we assumed a load resistance of 50 Ω. The diameter of the PD is 34 μm. The wavelength of the optical excitation is 1550 nm. The PD is excited from the top (from the n-side). The beamwidth of this normal excitation is the same as the PD diameter, 34 μm. We used a non-uniform mesh [22] with a maximum grid spacing of 1 nm for both steady-state and RF output power calculations. In broadband calculations, we set the time step size to 0.1 ps [23].

To assess the accuracy of our approach, we conducted a numerical study of the MUTC2. In the initial step of our study, we assumed a constant temperature of 300 K across the entire device and calculated the local electric fields and currents at a -5 V reverse bias. We then computed the local temperature changes in each cell of the mesh using Eq. (5). Since the device is illuminated from its n-side, we cumulatively summed these ∇T_i values to obtain the overall temperature change (ΔT) from the p-side to the n-side, as depicted by the blue curve in Fig. 2. Subsequently, we ran our drift-diffusion equations solver once more, this time assuming the local temperature as $T + \Delta T$. As shown by the red curve in Fig. 2, we now found a lower temperature distribution in the PD than the one estimated in the first iteration. We repeated this procedure five more times and observed that the temperature profile stabilized after the third iteration, i.e., $\Delta T < 0.001°$C.

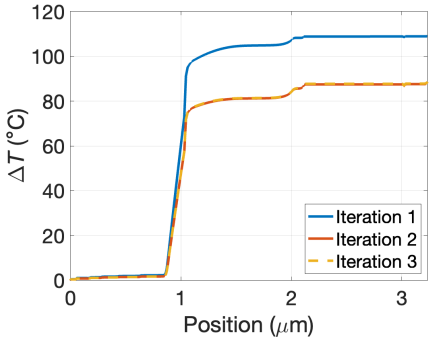

Fig. 2. Temperature distribution over the photodetector at the end of the first three iterations.

Figure 3 shows the calculated electric field distributions for each iteration. As expected, the electric field intensity is high inside the absorber (InGaAs) layers, where we also observe a dramatic change in the temperature profile. The main reason behind this sudden change in the temperature, Fig. 2), is that InGaAs has very low thermal conductivity, as shown in Fig. 1. This low thermal conductivity restricts the heat flow and leads to temperature build-up. Also note that we observe abrupt changes in the electric field intensity in Fig. 3. These changes occur when the material type changes and/or the doping concentration changes dramatically [1]–[3], [5], [7], [22], [23], [29]. For example in Fig. 3, around $z = 2\mu$m, high gradients in material properties and doping create sharp transitions in the electric field intensity.

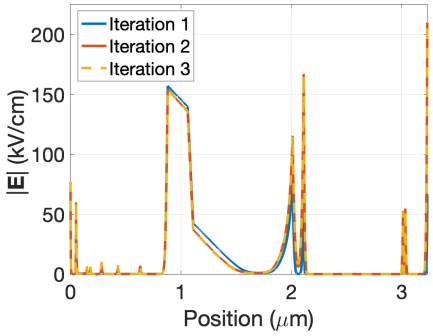

Fig. 3. Electric field distributions over the photodetector at the end of the first three iterations.

To delve further, we calculated the temperature, field, and current distributions over the photodetector, assuming a wide range of optical excitations. We assume that p-contact of the photodetector is maintained at 15°C. The temperature at the

n-contact as a function of dissipated power, as calculated by our model, is depicted by the blue curve in Fig. 4. The black squares denote the experimental measurements [4], while the red dashed curve represents simulation results obtained using a commercially available finite element method solver [4]. Overall, there exists a notable agreement among the numerical, experimental, and simulation outcomes. However, the disparity between numerical and experimental findings becomes more pronounced as power increases. Apart from our model's inherent approximation, several other factors could contribute to this deviation. For instance, the simplified geometry may not fully encapsulate the complexities of the actual device structure, or the boundary conditions for heat transfer may vary. At higher power levels, the convective heat transfer rate, which we have not incorporated, might escalate nonlinearly due to increased temperature differentials. A three-dimensional dynamic model that takes both conduction and convection currents into account is needed to increase accuracy.

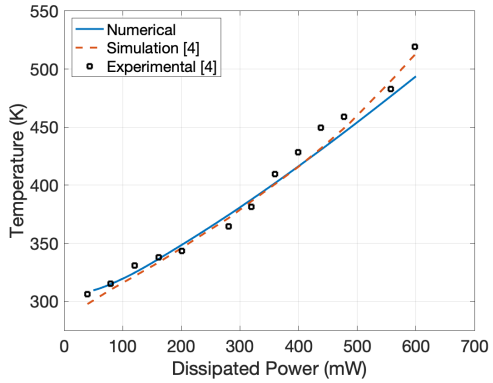

Fig. 4. Temperature of the n-contact as a function of dissipated power. Experimental and simulation results are taken from [4].

Although we did not integrate our dynamic drift-diffusion equations solver [22], [23] with a heat-transport model, we investigated how much difference would be observed in the results obtained by assuming a constant temperature distribution and a temperature distribution that varies according to Eq. (5).

We first set bias voltage (V_{b}) to 4 V and run our code at five incident power values (31 mW, 62 mW, 310 mW, 620 mW, and 930 mW) twice. In the first set, we assume that the temperature is constant, $T = 300$ K. In the second set, we use Eq. (5). As we increase the intensity of the incident light, we provide more photons to the photodetector, resulting in a higher number of generated electron-hole pairs. Consequently, in both cases, the photocurrent increases proportionally to the incident light intensity, as shown in Fig. 5 (a). However, the constant temperature (CT) approach estimates a higher amount of output current, nearly 12% more. In the varying temperature (VT) approach, these higher currents lead to higher temperatures, see Fig. 5 (b). In Fig. 5 (c), we plot the quantum efficiency calculated with both approaches, assuming the photodetector is covered with SiO_2 to match the refractive index of the fiber and minimize the reflectance from the device. The CT approach estimates the quantum efficiency to be close to 0.65, whereas the measured value is reported as 0.55 [5]. The estimate of the VT approach, ~ 0.53, is much closer to this experimental result. We should note that since the mobilities decrease, one might expect quantum efficiency to drop with increasing temperature. However, the narrowing of the bandgap with increasing temperature allows more photons to excite electrons. Additionally, the presence of more thermally-excited charge carriers at higher temperatures provides more carriers available for generation by incident photons. As a result, we observe a slight increase in quantum efficiency, as seen in the blue curve in Fig. 5(c), similar to the experiment results provided in [30]. Next, we plot the phase noise calculated in Fig. 5(d). The modulation frequency and depth are 9 GHz and 100%, respectively. Since the phase noise generally decreases with increasing currents, in both approaches, we first observe a decay in the phase noise, then it starts to converge. The phase noise calculated with the VT model is $8 - 10$ dBc/Hz higher than the constant temperature approach. In Fig. 5(e), the continuous and dashed lines represent the broadband RF output power calculated at the five aforementioned incident power levels for modulation frequencies from 0 to 40 GHz using VT and CT approaches, respectively. In all cases, RF output power first increases with modulation frequency, then decreases. However, the frequency where RF output becomes the maximum is higher for VT results than the CT results. In Fig. 5(f), we plot the bandwidths as a function of incident power. The CT approach estimates the bandwidth to be around 16.5 GHz at low modulation frequencies and then decreases, whereas the VT approach estimates much higher bandwidths, initially to be 23.9 GHz and then decreases to lower values. The experimentally reported value is 24 GHz [5]. Again, we observe that the VT approach provides a more realistic outcome.

Next, we investigated the impact of the approximate temperature distribution on the performance of the photodetector while it produces the same photocurrent as we allow the reverse bias to vary. We followed our VT approach, assuming six different reverse bias values (1.5 V, 2.5 V, 4.7 V, 8.4 V, 12 V, and 15 V). For each bias value, a stable output photocurrent of 40 mA was obtained, as shown in Fig. 6(a), by adjusting the incident power as depicted in Fig. 6(b), similar to [4]. Figures 6(c) and (d) illustrate that both the temperature and electric field intensity inside the absorber layers increases with the rising bias voltage. These increasing electric fields accelerate the charge carriers, reducing their transit time through the photodetector. A reduced transit time spread leads to lower phase noise up to a certain point, as depicted in Fig. 6(e).

The quantum efficiency of the photodetector, as shown in Fig. 6(f), slightly increases from 0.518 to 0.532 in the opposite direction to the decreasing incident power depicted in Fig. 6(b). At high power levels, where the incident power is close to 1 W, the photodetector is close to a point where it becomes saturated, and additional incident photons do not result in a proportional increase in the generated electron-hole pairs. In Fig. 6(g), we observe that the bandwidth of the photodetector first increases and then decreases with bias voltage, similar to the results presented in [9], [30], [31]. This nonlinear dependence on the bias voltage can be explained as follows:

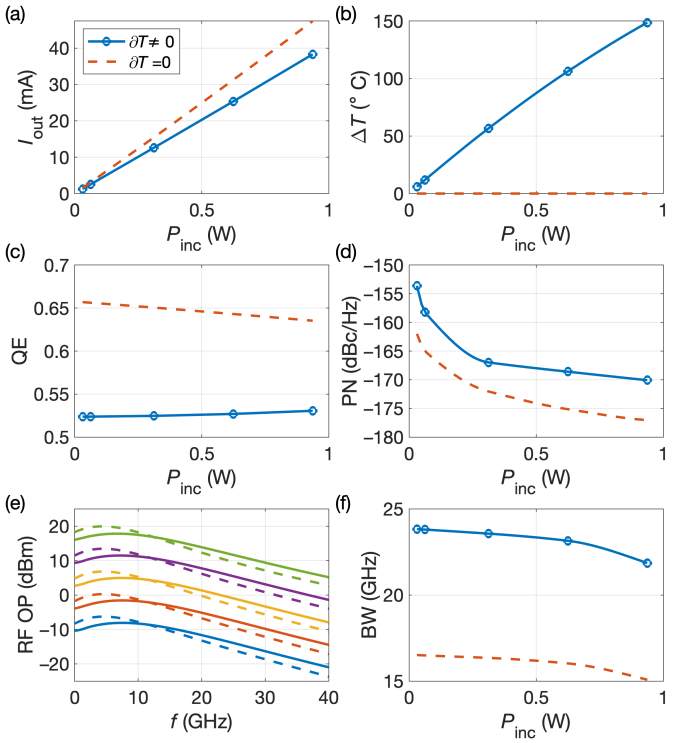

Fig. 5. (a) Output current, (b) temperature change at the n-contact, (c) quantum efficiency, (d) phase noise, (e) RF output power, and (f) bandwidth of the MUTC2 calculated by assuming a constant temperature (dashed curves) vs. varying temperature (solid curves).

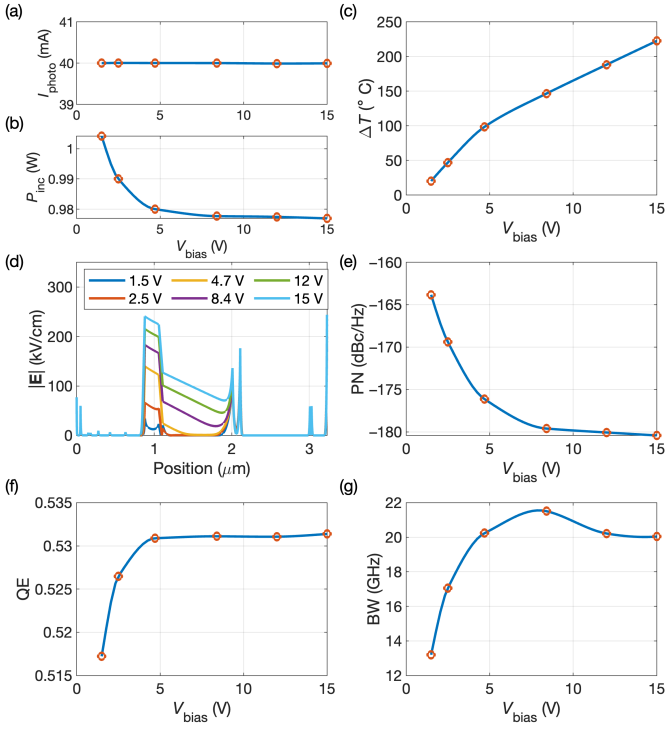

Fig. 6. (a) MUTC2 photodetector produces the same photocurrent (I_{photo}) at different reverse biases (V_{b}) by adjusting the incident power (P_{inc}) to the values depicted in (b). (c) The temperature change (ΔT) at the n-contact, (d) electric field distributions, (e) phase noise, (f) quantum efficiency, and (g) bandwidth with increasing V_{b} as a function of reverse bias voltage.

the temperature dependence of bandwidth is influenced by competing effects. As temperature rises, the bandgap narrows, allowing electrons to be excited with less energy, resulting in a wider bandwidth. However, the increased number of carriers generated by thermal energy at higher temperatures also leads to increased carrier recombination, which reduces the response time and bandwidth of the photodetector. The balance between these two competing effects determines the temperature dependence of the photodetector's bandwidth. If the goal is to obtain the widest bandwidth while producing an output current of 40 mA, then the modulation frequency of 7.8 GHz would be the ideal choice.

IV. Discussions

In this study, we assume a constant temperature at the bottom of the photodetector (at $z = 0$). However, the proposed method can readily be extended to investigate photodetectors positioned above a heat sink [4]. To accomplish this extension, one needs to use a negative H heat source term, calculate the temperature reduction in the opposite direction (from p-contact to n-contact), and determine the overall change in each layer of the mesh by adding forward (positive) and backward (negative) terms. Nonetheless, the placement of MUTC2 over a heat sink is not anticipated to yield a substantial enhancement in device performance for two primary reasons: (i) heating in the p-region is not severe, and (ii) the low thermal conductance of InGaAs impedes cooling in the n-region. Consequently, encasing a heat sink around the n-region would represent a more efficacious approach, albeit beyond the scope of our 1D solver.

As mentioned in [3], appropriately managing the externally controllable parameters such as the intensity, wavelength, and modulation frequency of the optical excitation and applied reverse bias voltage is necessary to obtain the optimal performance from a photodetector. It is also necessary to properly design the thickness and doping concentration of the layers forming the p and i regions. One can use modern numerical optimization techniques to determine the optimum values for the layer thicknesses and doping concentrations, similar to [29]. Due to its relatively high electron mobility, high sensitivity in the near-infrared region, and bandgap-tunability by adjusting the composition of indium and gallium, InGaAs has become the principal semiconductor that is used to design UTC and MUTC PDs, but its very low thermal conductivity is a serious drawback. Using InGaAsP or other types of alloys, it may be possible to design PDs with more efficient heat dissipation while keeping the other performance metrics nearly the same.

As previously stated, the proposed model lacks dynamic effects. In its present configuration, the model represents a straightforward yet effective methodology for investigating photodetectors in their steady-state under continuous excitations. Nevertheless, in scenarios where photodetectors receive intense pulsed optical signals, the duty cycle and repetition rate of the pulses can profoundly influence temperature dynamics. The swift heating and cooling cycles inherent in

pulse operation may induce substantial alterations in device performance. Hence, one would need a dynamic model to study photodetectors excited with pulsed optical signals.

V. Conclusions

In conclusion, this study introduces a simple yet effective method for approximating the temperature distribution in photodetectors operating under steady-state conditions. Utilizing a simplified heat transport model, we investigate the implications of temperature variations on crucial performance metrics such as quantum efficiency, bandwidth, and phase noise. This approach yields valuable insights into the intricate interplay between temperature and photodetector performance.

The numerical results reveal significant departures from the conventional assumption of constant room temperature operation. Specifically, our findings highlight that assuming constant temperature tends to overestimate output current and quantum efficiency, while underestimating bandwidth. Conversely, our model, considering varying temperature, aligns closely with measured values for quantum efficiency and bandwidth. Notably, the low thermal conductivity of InGaAs emerges as a critical factor influencing temperature build-up and subsequent performance variations. Furthermore, the exploration of temperature-dependent changes under varying reverse bias voltage elucidates nonlinear trends in bandwidth, phase noise, and quantum efficiency.

The numerical model presented here, validated against experimental data, contributes to a comprehensive understanding of the thermal management and optimization strategies essential for advancing high-power, high-linearity photodiodes in photonic microwave applications. This work lays the groundwork for further investigations and advancements in the thermal characterization of advanced photodetectors that are typically used in high-power applications.

References

[1] K. Williams, R. Esman, and M. Dagenais, "Effects of high space-charge fields on the response of microwave photodetectors," *IEEE Photon. Tech. L.*, vol. 6, no. 5, pp. 639–641, 1994.

[2] T. Ishibashi, T. Furuta, H. Fushimi, S. Kodama, H. Ito, T. Nagatsuma, N. Shimizu, and Y. Miyamoto, "InP/InGaAs uni-traveling-carrier photodiodes," *IEICE Trans. Electron.*, vol. 83, no. 6, pp. 938–949, 2000.

[3] D.-H. Jun, J.-H. Jang, and J.-I. Song, "Effect of temperature on bandwidth and responsivity of uni-traveling-carrier and modified uni-traveling-carrier photodiodes," *Jpn. J. Appl. Phys.*, vol. 46, no. 4S, p. 2360, 2007.

[4] Z. Li, Y. Fu, M. Piels, H. Pan, A. Beling, J. E. Bowers, and J. C. Campbell, "High-power high-linearity flip-chip bonded modified uni-traveling carrier photodiode," *Opt. Express*, vol. 19, no. 26, pp. B385–B390, 2011.

[5] Z. Li, H. Pan, H. Chen, A. Beling, and J. C. Campbell, "High-saturation-current modified uni-traveling-carrier photodiode with cliff layer," *IEEE J. Quantum Electron.*, vol. 46, no. 5, pp. 626–632, 2010.

[6] N. Li, X. Li, S. Demiguel, X. Zheng, J. Campbell, D. Tulchinsky, K. Williams, T. Isshiki, G. Kinsey, and R. Sudharsansan, "High-saturation-current charge-compensated InGaAs-InP uni-traveling-carrier photodiode," *IEEE Photon. Tech. L.*, vol. 16, no. 3, pp. 864–866, 2004.

[7] A. Beling, X. Xie, and J. C. Campbell, "High-power, high-linearity photodiodes," *Optica*, vol. 3, pp. 328–338, Mar 2016.

[8] C. Moseley *et al.*, "Investigation of modified uni-traveling carrier photodiode for cryogenic microwave photonic links," *Opt. Continuum*, vol. 2, pp. 2215–2224, Oct 2023.

[9] G. Zhou and P. Runge, "Nonlinearities of high-speed p-i-n photodiodes and MUTC photodiodes," *IEEE Trans. Microw. Theory Tech.*, vol. 65, no. 6, pp. 2063–2072, 2017.

[10] K. Kato, "Ultrawide-band/high-frequency photodetectors," *IEEE Trans. Microw. Theory Techn.*, vol. 47, no. 7, pp. 1265–1281, 1999.

[11] X. Wang, N. Duan, H. Chen, and J. C. Campbell, "InGaAs–InP photodiodes with high responsivity and high saturation power," *IEEE Photon. Tech. L.*, vol. 19, no. 16, pp. 1272–1274, 2007.

[12] K. Józwikowski, C. Musca, L. Faraone, and A. Józwikowska, "A detailed theoretical and experimental noise study in n-on-p $Hg_{0.68}Cd_{0.32}Te$ photodiodes," *Solid-State Electronics*, vol. 48, no. 1, pp. 13–21, 2004.

[13] K. Jóźwikowski, M. Kopytko, A. Rogalski, and A. Jóźwikowska, "Enhanced numerical analysis of current-voltage characteristics of long wavelength infrared n-on-p hgcdte photodiodes," *J. Appl. Phys.*, vol. 108, no. 7, 2010.

[14] H. Z. Fardi, D. W. Winston, R. E. Hayes, and M. C. Hanna, "Numerical modeling of energy balance equations in quantum well Al_x /Ga_{1-x}/As/GaAs pin photodiodes," *IEEE Transactions on Electron Devices*, vol. 47, no. 5, pp. 915–921, 2000.

[15] G. Li, N. André, O. Poncelet, P. Gérard, S. Z. Ali, F. Udrea, L. A. Francis, Y. Zeng, and D. Flandre, "Silicon-on-insulator photodiode on micro-hotplate platform with improved responsivity and high-temperature application," *IEEE Sensors Journal*, vol. 16, no. 9, pp. 3017–3024, 2016.

[16] J. Rosbeck, R. Starr, S. Price, and K. Riley, "Background and temperature dependent current-voltage characteristics of HgCdTe photodiodes," *J. Appl. Phys.*, vol. 53, no. 9, pp. 6430–6440, 1982.

[17] P. Dalapati, N. B. Manik, and A. N. Basu, "Effect of temperature on electro-optical characteristics of silicon based pn photodiode (vtb8440bh)," *Silicon*, vol. 10, pp. 2547–2553, 2018.

[18] M. Brunk and A. Jüngel, "Simulation of thermal effects in optoelectronic devices using coupled energy-transport and circuit models," *Math. Models Methods Appl. Sci.*, vol. 18, no. 12, pp. 2125–2150, 2008.

[19] A. R. Wichman, R. E. DeWames, and E. Bellotti, "Three-dimensional numerical simulation of planar p+ n heterojunction $In_{0.53}Ga_{0.47}As$ photodiodes in dense arrays Part I: Dark current dependence on device geometry," in *Infrared Technology and Applications XL*, vol. 9070, pp. 10–30, SPIE, 2014.

[20] I. Pisarenko and E. Ryndin, "Numerical drift-diffusion simulation of GaAs pin and Schottky-barrier photodiodes for high-speed AIIIBV on-chip optical interconnections," *Electronics*, vol. 5, no. 3, p. 52, 2016.

[21] S. A. Malyshev, A. L. Chizh, and Y. G. Vasileuski, "High-power InGaAs/InP partially depleted absorber photodiodes for microwave generation," *J. Lightwave Technol.*, vol. 26, no. 15, pp. 2732–2739, 2008.

[22] E. Simsek, I. M. Anjum, and C. R. Menyuk, "Solving drift diffusion equations on non-uniform spatial and temporal domains," in *2023 Photonics & Electromagnetics Research Symposium (PIERS)*, pp. 1644–1651, 2023.

[23] E. Simsek, I. M. Anjum, T. F. Carruthers, C. R. Menyuk, J. C. Campbell, D. A. Tulchinsky, and K. J. Williams, "Fast evaluation of rf power spectrum of photodetectors with windowing functions," *IEEE Trans. Electron. Dev.*, vol. 70, no. 7, pp. 3643–3648, 2023.

[24] W. Kim, J. Zide, A. Gossard, D. Klenov, S. Stemmer, A. Shakouri, and A. Majumdar, "Thermal conductivity reduction and thermoelectric figure of merit increase by embedding nanoparticles in crystalline semiconductors," *Phys. Rev. Lett.*, vol. 96, p. 045901, Feb 2006.

[25] D. K. Gaskill, N. Bottka, L. Aina, and M. Mattingly, "Band-gap determination by photoreflectance of InGaAs and InAlAs lattice matched to InP," *Appl. Phys. Lett.*, vol. 56, pp. 1269–1271, 03 1990.

[26] S. M. Sze, Y. Li, and K. K. Ng, *Physics of Semiconductor Devices*. John wiley & sons, 2021.

[27] M. Sotoodeh, A. H. Khalid, and A. A. Rezazadeh, "Empirical low-field mobility model for III–V compounds applicable in device simulation codes," *J. Appl. Phys.*, vol. 87, pp. 2890–2900, 03 2000.

[28] R. Quay, C. Moglestue, V. Palankovski, and S. Selberherr, "A temperature dependent model for the saturation velocity in semiconductor materials," *Mater. Sci. Semicond. Process.*, vol. 3, no. 1, pp. 149–155, 2000.

[29] I. M. Anjum, E. Simsek, S. E. J. Mahabadi, T. F. Carruthers, C. R. Menyuk, J. C. Campbell, D. A. Tulchinsky, and K. J. Williams, "Use of evolutionary optimization algorithms for the design and analysis of low bias, low phase noise photodetectors," *J. Lightwave Technol.*, vol. 41, no. 23, pp. 7285–7291, 2023.

[30] M. Chtioui, F. Lelarge, A. Enard, F. Pommereau, D. Carpentier, A. Marceaux, F. van Dijk, and M. Achouche, "High responsivity and high power UTC and MUTC GaInAs-InP photodiodes," *IEEE Photonic Tech. L.*, vol. 24, no. 4, pp. 318–320, 2012.

[31] Y. Chen, Z. Xie, J. Huang, Z. Deng, and B. Chen, "High-speed uni-traveling carrier photodiode for 2 μm wavelength application," *Optica*, vol. 6, pp. 884–889, Jul 2019.